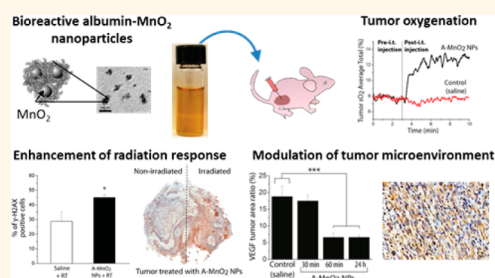# Multifunctional Albumin−MnO$_2$ Nanoparticles Modulate Solid Tumor Microenvironment by Attenuating Hypoxia, Acidosis, Vascular Endothelial Growth Factor and Enhance Radiation Response

Preethy Prasad,[†,⊥] Claudia R. Gordijo,[†,⊥] Azhar Z. Abbasi,[†] Azusa Maeda,[‡] Angela Ip,[†] Andrew Michael Rauth,[§] Ralph S. DaCosta,[‡,*] and Xiao Yu Wu[†,*]

[†]Department of Pharmaceutical Sciences, Leslie L. Dan Faculty of Pharmacy, University of Toronto, Toronto, Ontario M5S 3M2, Canada, [‡]Princess Margaret Cancer Center, The Campbell Family Institute for Cancer Research, University Health Network, 610 University Avenue, Toronto, Ontario M5G 2M9, Canada, and [§]Department of Medical Biophysics, University of Toronto, 610 University Avenue, Toronto, Ontario M5G 2M9, Canada. [⊥]P.P. and C.R.G. contributed equally to this work.

ABSTRACT Insufficient oxygenation (hypoxia), acidic pH (acidosis), and elevated levels of reactive oxygen species (ROS), such as H$_2$O$_2$, are characteristic abnormalities of the tumor microenvironment (TME). These abnormalities promote tumor aggressiveness, metastasis, and resistance to therapies. To date, there is no treatment available for comprehensive modulation of the TME. Approaches so far have been limited to regulating hypoxia, acidosis, or ROS individually, without accounting for their interdependent effects on tumor progression and response to treatments. Hence we have engineered multifunctional and colloidally stable bioinorganic nanoparticles composed of polyelectrolyte−albumin complex and MnO$_2$ nanoparticles (A-MnO$_2$ NPs) and utilized the reactivity of MnO$_2$ toward peroxides for regulation of the TME with simultaneous oxygen generation and pH increase. *In vitro* studies showed that these NPs can generate oxygen by reacting with H$_2$O$_2$ produced by cancer cells under hypoxic conditions. A-MnO$_2$ NPs simultaneously increased tumor oxygenation by 45% while increasing tumor pH from pH 6.7 to pH 7.2 by reacting with endogenous H$_2$O$_2$ produced within the tumor in a murine breast tumor model. Intratumoral treatment with NPs also led to the downregulation of two major regulators in tumor progression and aggressiveness, that is, hypoxia-inducible factor-1 alpha and vascular endothelial growth factor in the tumor. Combination treatment of the tumors with NPs and ionizing radiation significantly inhibited breast tumor growth, increased DNA double strand breaks and cancer cell death as compared to radiation therapy alone. These results suggest great potential of A-MnO$_2$ NPs for modulation of the TME and enhancement of radiation response in the treatment of cancer.

KEYWORDS: multifunctional nanoparticles · manganese dioxide · modulating tumor microenvironment · hypoxia · acidosis · HIF-1 · VEGF · radiation response · breast cancer

I n solid tumors hypoxia (low oxygenation) often occurs as a consequence of a disrupted balance between the supply and consumption of O$_2$, owing in part to tumor growth and vascular abnormalities, the latter also affecting O$_2$ transport insufficiencies.[1] Hypoxia, a characteristic of the tumor microenvironment (TME), has been shown to contribute to the resistance to radiation therapy (RT) and to promote clinically aggressive phenotypes in cancer.[2,3] Studies have demonstrated that nearly 40% of breast cancers exhibit tumor regions with oxygen concentrations below that required for half maximal radiosensitivity, reducing the effectiveness of radiation therapy.[4]

Hypoxia also leads to chronic over activation of hypoxia-inducible-factor-1 (HIF-1) which plays a pivotal role in adaptive responses to hypoxia by modulating various cellular functions like proliferation, apoptosis, angiogenesis, pH balance, and anaerobic glycolysis.[5,6] Upon activation, HIF-1 binds to the hypoxic responsive element,

thereby promoting transcription of various genes including VEGF (vascular endothelial growth factor) and genes encoding for glucose transporters.[7] The expression of VEGF further induces angiogenesis and plays a key role in promoting malignant tumor growth.[8,9] HIF-1 also mediates the switch from aerobic to anaerobic metabolism in hypoxic tumors for energy preservation by activating glucose transporters and glycolytic enzymes leading to an increase in levels of lactic acid and acidosis (lower extracellular pH, pHe < 6.9).[10,11] In addition, hypoxia and high proliferation of cancer cells produce excess amounts of reactive oxygen species (ROS), for example, hydrogen peroxide (H_2O_2).[12] Together, hypoxia, acidosis, and ROS promote mutagenesis, metastasis of cancer cells, angiogenesis, and resistance to therapies, contributing to treatment failure.

To date, various strategies have been proposed to modify the TME, aimed at the (systemic) improvement of tumor oxygenation to surmount hypoxia-associated radioresistance. These strategies include hyperbaric oxygen therapy,[13] artificial blood substitutes,[14] and drugs which preferentially kill or sensitize hypoxic cells to radiation.[15] Unfortunately, the utility of such methods in clinical settings is limited because of safety concerns, reagent stability, and/or inconsistent clinical response. Therefore, there is a continued and urgent need for new strategies to improve tumor oxygenation in vivo to enhance the radiation response in solid tumors.

Here, we have taken advantage of the high reactivity and specificity of manganese dioxide nanoparticles (MnO_2 NPs) toward H_2O_2 for the simultaneous and sustained production of O_2 and regulation of pH[16,17] to modulate the TME. Unlike other strategies to increase tumor oxygenation, mostly by the delivery of molecular oxygen by nanoparticles with limited O_2 loading capacity,[2] MnO_2 NPs are able to generate O_2 in situ for a prolonged time by reacting with undesirable and abundantly available tumor metabolites (H_2O_2 and H^+). Another advantage of MnO_2 NPs is their dual functions as both catalyst and reactant. In the latter case, they are decomposed to harmless, water-soluble Mn^{2+} ions,[17] avoiding the in vivo accumulation of the metal oxide commonly observed for other metal-based nanoparticle (NP) systems.[18] Compared with other metal nanoparticles extensively explored for biological applications, MnO_2 NPs have been limited to use in biochemical sensors[17,19] and bioassays.[20] To our knowledge, their reactivity toward tumor H_2O_2 has not been studied for in vivo ROS reduction, O_2 production, or for the regulation of pH in biological systems. Therefore, for the first time, the development and in vivo characterization of MnO_2 NPs are reported for simultaneous modulation of hypoxia and acidosis of the TME, and for enhancement of ionizing radiation-induced tumor cell cytotoxicity in a murine breast tumor animal model.

RESULTS AND DISCUSSION

Preparation of A-MnO₂ NPs. For the synthesis of NPs, we employed a one-step method to reduce manganese permanganate ($KMnO_4$) to MnO_2 NPs with cationic polyelectrolyte poly(allylamine hydrochloride) (PAH). This synthesis procedure is rapid, reproducible, and gives stable MnO_2 colloidal dispersions with an average NP size distribution of 15 nm (Figure 1a,b). In the present synthesis method, we were able to decrease by 50% the amount of PAH normally used in polyelectrolyte-based NPs synthesis,[21] as shown in the ultraviolet−visible (UV−vis) spectrum of samples prepared with various polyelectrolyte ratios (Figure 1c). The decrease in the amount of PAH utilized in the NP formulation is very important for in vivo applications, since cationic polyelectrolytes can show pronounced concentration-dependent cytotoxicity. The polyelectrolyte used here served not only as a reducing reagent to reduce $KMnO_4$ to MnO_2, but also as a protective layer to stabilize as-formed NPs due to electrostatic repulsion (zeta potential, +30 mV, Figure 1d).

To formulate MnO_2 nanoparticles for biomedical in vivo applications we took into account the issues of nanoparticle stability, size control, and toxicity. For biological applications, NPs must be stable in cell culture medium or normal saline required for in vitro and in vivo studies, respectively. Polyelectrolyte-coated MnO_2 nanoparticles are too small and positively charged, which can cause high instability in cell medium or saline and result in toxicity. To solve these problems, we have conjugated small polyelectrolyte-coated MnO_2 nanoparticles with bovine serum albumin (BSA) and obtained particles of suitable size, charge, colloidal stability, and biocompatibility for in vitro and in vivo applications, while maintaining the MnO_2 reactivity toward H_2O_2 for the production of oxygen and increase in pH. BSA can form stable noncovalent complexes with cationic polyelectrolytes,[22] leading to lower NP toxicity.[23] The MnO_2 NP-albumin conjugates (A-MnO_2) prepared were approximately 50 nm in size (Figure 1b), negatively charged (−25 mV) (Figure 1d) and stable in alpha minimal essential medium (αMEM) cell medium and saline (Figure 1e), making them suitable for in vivo applications. The albumin coating also provided the NPs with different surface charge and chemistry allowing us to further functionalize the NP surface with protein-reactive fluorescent dyes such as Texas Red (excite 596/emit 617 nm) and amine-reactive near-infrared dye (excite 754/emit 778 nm). These fluorescence-labeled NPs were utilized in our subsequent in vitro and in vivo studies.

Multifunctionality of A-MnO₂ NPs in Culture Medium. We first investigated the multifunctionality of the A-MnO_2 NPs to generate O_2 and to increase the medium pH in vitro upon reaction with H_2O_2 at endogenous levels. The reaction between MnO_2 and H_2O_2 is a complex reaction leading to the decomposition of H_2O_2 and the
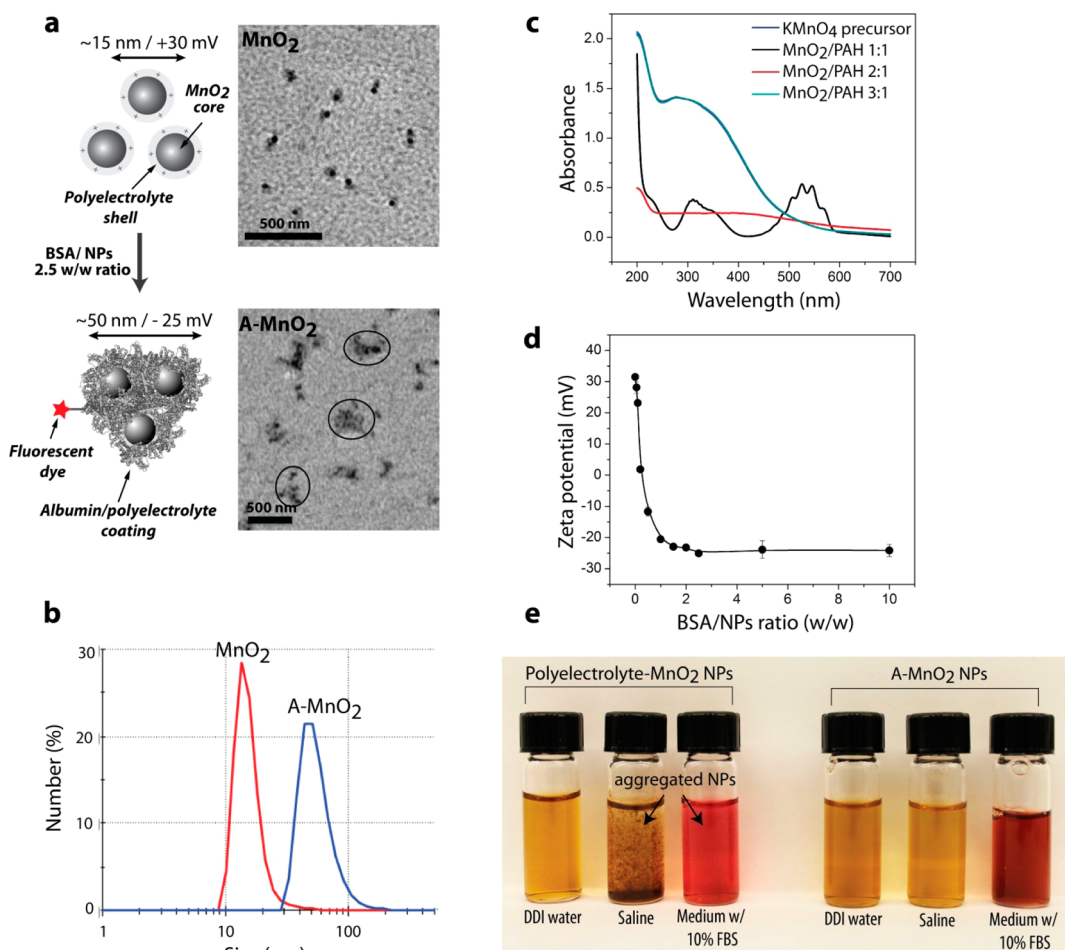
Figure 1. Characterization of A-MnO$_2$ NPs: (a) Diagram and TEM images of MnO$_2$ and A-MnO$_2$ NPs. Precursor MnO$_2$ NPs (~15 nm) are stabilized by positively charged PAH. In A-MnO$_2$ (~50 nm) several MnO$_2$ particles are entrapped in a PHA/BSA complex due to strong electrostatic interaction between the protein and the polymer. (b) Size distribution of NPs. (c) UV–vis absorption spectra of KMnO$_4$ solution and MnO$_2$ NPs prepared at various molar ratios between PAH and MnO$_2$. After the reaction with PAH at ratios 2:1 and 3:1, the KMnO$_4$ peaks (315, 525, and 545 nm) disappeared, and a new broad peak around 300 nm appeared for these samples, an indicator of the formation of MnO$_2$ nanoparticles. The new peak around 300 nm is attributed to the surface plasmon band of colloidal manganese dioxide.[21] (d) Effect of coating of MnO$_2$ NPs with BSA on zeta potential for various BSA/NPs ratios. By adding BSA to a MnO$_2$ NP aqueous suspension, the zeta potential of the NPs decreased from +30 mV to −25 mV. (e) Picture of polyelectrolyte MnO$_2$ NPs (left) and A-MnO$_2$ NPs (right) (1 mM) in various aqueous media: DDI water, normal saline (0.9% NaCl), and αMEM cell medium containing 10% fetal bovine serum (FBS). MnO$_2$ NPs undergo aggregation in saline or cell culture medium, while A-MnO$_2$ NPs are stable in these media. The red color observed in the vials comes from the pH indicator in the αMEM medium.

production of O$_2$ as summarized in Figure 2a. Besides the production of O$_2$, the reaction causes an increase in the local pH by the consumption of H$^+$ ions and the production of an intermediate Mn-oxo-hydroxide (MnOOH).[17] This phenomenon can be particularly useful for the regulation of local pH in cancer cells and tumor tissue. Hence we studied if A-MnO$_2$ NPs would generate measurable amounts of oxygen and increase pH at low concentrations of H$_2$O$_2$ found in the human body (i.e., 100 μM and up to 1 mM).[24] We found that at a very low concentration (~45 μM of MnO$_2$), the NPs were able to completely quench 1 mM H$_2$O$_2$ in cell medium within 40 min (Figure 2b). We further investigated the O$_2$ generating properties of the NPs using an in-house-made hypoxia-maintaining chamber coupled with both a commercially available oxygen probe and a

pH microelectrode. Significant amounts of O$_2$ were produced (Figure 2c) accompanied by an increase in the pH of physiological buffer (phosphate/saline buffer) by one pH unit from pH 6.8 to pH 7.8 (Figure 2d) by the reaction of 45 μM of MnO$_2$ with 250 μM H$_2$O$_2$. In an attempt to simulate in vivo conditions where H$_2$O$_2$ is continuously generated by tumor cells, we measured the O$_2$ production by the NPs during the continuous addition of exogenous H$_2$O$_2$ (250 μM) into the chamber every 30 min. We observed that a single dose of the NPs (90 μM MnO$_2$) continuously generated O$_2$ for at least six cycles of 30 min each (Figure 2e). These results demonstrated that H$_2$O$_2$ and protons can diffuse rapidly across the polyelectrolyte–albumin complex, access the reactive sites of the MnO$_2$ cores, produce O$_2$, and increase pH in a sustained manner under hypoxic conditions.
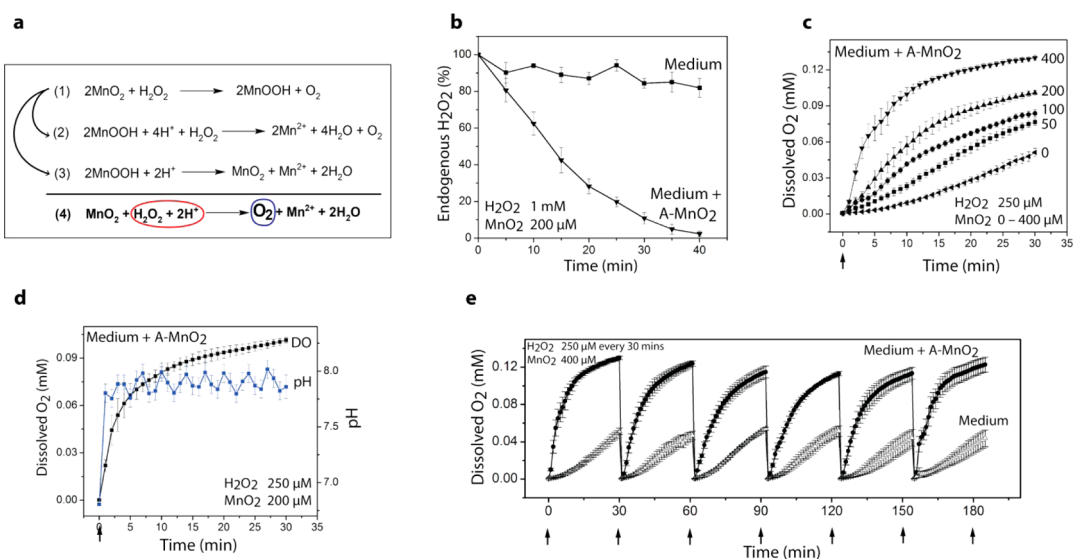
Figure 2. *In vitro* reactivity of A-MnO$_2$ NPs toward hydrogen peroxide: (a) Reaction scheme showing the reactivity of MnO$_2$ toward H$_2$O$_2$ for the production of O$_2$ and removal of protons. (b) Quenching of endogenous level H$_2$O$_2$ (1 mM) by A-MnO$_2$ NPs (45 μM). (c) Oxygen generation at various A-MnO$_2$ NP contents (numbers indicate MnO$_2$ in μM). (d) Simultaneous O$_2$ generation and pH increase vs time by the A-MnO$_2$ NPs. (e) O$_2$ generation by addition of H$_2$O$_2$ to an A-MnO$_2$ NP suspension. All experiments were performed (n = 3) in cell culture medium containing 10% FBS at 37 °C. Error bars are standard error of the mean.

Uptake of A-MnO$_2$ NPs by Breast Cancer Cells. It is known that the aberrant metabolism of cancer cells leads to significantly elevated cellular concentrations of H$_2$O$_2$.[12] We hypothesized that if the NPs could be taken up by cancer cells, they could react quickly with endogenous H$_2$O$_2$ produced by cancer cells under hypoxic stress, thus producing O$_2$ *in situ*. To test this hypothesis, we first examined the cellular uptake of the NPs by incubating EMT6 murine breast cancer cells with fluorescence-labeled A-MnO$_2$ NPs, and observed significant cellular uptake of NPs within 60 min of incubation (Figure 3a). This finding was confirmed by transmission electron microscopy (TEM). TEM images (Figure 3b) showed EMT6 cells *in vitro* underwent membrane invagination and engulfment of the NPs, and the NPs taken up by the cell were distributed within the cell cytoplasm and vesicles after 1 h incubation.

This effective cellular uptake of A-MnO$_2$ NPs may be attributable to the interaction of albumin-saturated NPs (Figure 1d) with albumin receptor gp60 and/or the albumin-binding protein SPARC (secreted protein, acidic and rich in cysteine) overexpressed on the cancer cells, which have been found to be responsible for tumor targeting and cancer cell uptake of albumin-bound taxanes and other albumin-based NPs.[25−28] Nevertheless, confirmation of this mechanism is outside the scope of the present work and will be conducted in future experiments.

Oxygen Generation in the Presence of Hypoxic Cancer Cells. We found that the NPs incubated with hypoxic breast cancer cells could react quickly with endogenous H$_2$O$_2$ produced by the cells under hypoxic stress, thus producing O$_2$ *in situ* (Figure 3c). Significant amounts of O$_2$ (∼6-fold increase of O$_2$ levels in the medium)

were detected within 2 min by reacting with H$_2$O$_2$ released by the cancer cells (Figure 3c). These results indicate that the endogenous levels of H$_2$O$_2$ released by hypoxic cancer cells *in vitro* is sufficient to react with the NPs and generate measurable O$_2$ without the addition of exogenous H$_2$O$_2$ to the culture medium. Moreover, at the concentration used for *in vitro* O$_2$ generation (45 μM MnO$_2$), A-MnO$_2$ NPs showed relatively low cytotoxicity to EMT6 cancer cells (∼80% cell viability) (Figure 3d). On the basis of these data, we hypothesize that elevated levels of H$_2$O$_2$ in solid tumors could serve as a reactant for O$_2$ production *in vivo*.

Effect of A-MnO$_2$ NPs on Tumor Oxygenation. The effect of A-MnO$_2$ NPs on oxygen saturation within orthotopic murine EMT6 cell breast tumors was assessed with a small animal photoacoustic (PA) imaging system following intratumoral (i.t.) injection of 50 μL of A-MnO$_2$ NP suspension in saline. PA imaging measures vascular saturated O$_2$ (sO$_2$) by the differential optical absorption of oxygenated and deoxygenated hemoglobin at different wavelengths, which is directly correlated with changes in O$_2$ concentration in the blood.[29] To ensure similar localization of the NPs in each tumor we used ultrasound image-guidance to inject the NPs into the tumor *in vivo*. Since the blood vessels maintain a saturated level of oxygen under normoxic conditions, the mice were maintained under 7% O$_2$ during the experiments to visualize the enhancement of oxygen production by the A-MnO$_2$ NPs. We measured vascular sO$_2$ before and after i.t. injections of A-MnO$_2$ NPs suspension or saline only (control) and found that sO$_2$ increased promptly by approximately 45% as compared with control tumors (Figure 4a−c). It is
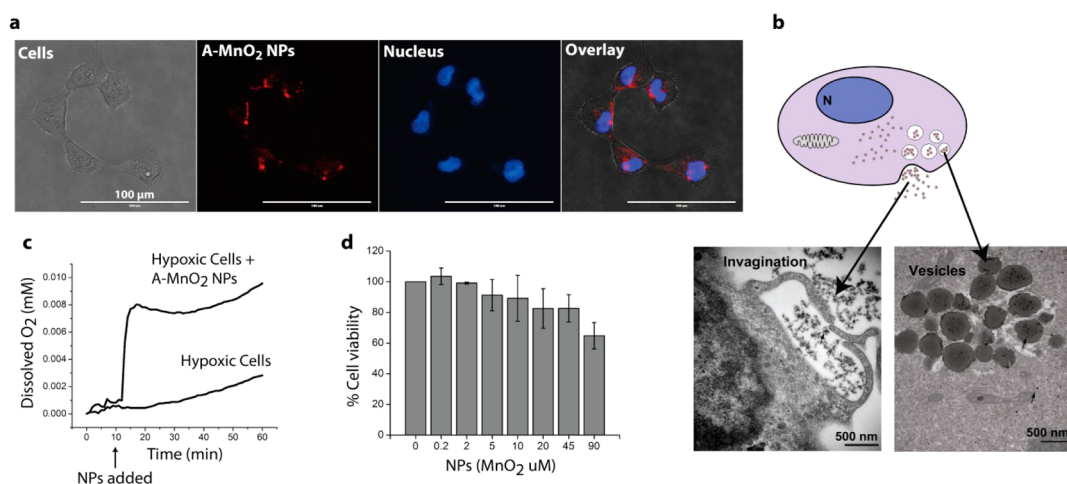
Figure 3. Cellular uptake, cellular oxygen generation, and cytotoxicity of A-MnO$_2$ NPs: (a) Fluorescence images of cellular uptake of A-MnO$_2$ NPs at 37 °C by murine EMT6 breast cancer cells following 1 h incubation with NPs. (b) TEM images of cellular uptake of A-MnO$_2$ NPs. (c) O$_2$ generation by A-MnO$_2$ NPs incubated with hypoxic cancer cells ($n = 3$). Suspended cells are made hypoxic and upon addition to A-MnO$_2$ to the culture oxygen is generated by the reactivity of NPs toward H$_2$O$_2$ released by hypoxic cancer cells. (d) Viability of murine EMT6 cancer cells (10^5 cells/mL) exposed to various concentrations of A-MnO$_2$ NPs for 48 h. Percent of cell viability was determined with MTT assay. ($n = 3$) Error bars represent standard errors of the mean.
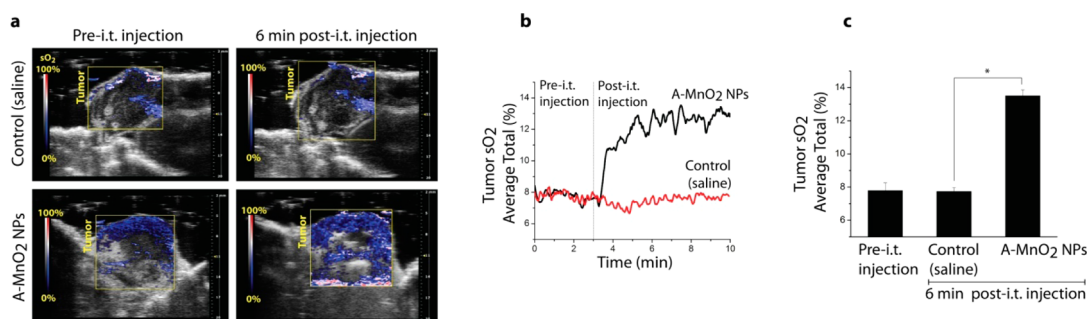

Figure 4. Effect of A-MnO$_2$ NPs on tumor oxygenation: (a) Representative 2D photoacoustic images of EMT6 solid tumors showing parametric map of estimated oxygen saturation (sO$_2$) pre- and post-i.t. injection of saline (control) or A-MnO$_2$ NPs. (b) Average total sO$_2$ in the tumor over time. (c) Comparison of average tumor sO$_2$ levels before and after treatments ($n = 3$). Error bars represent standard errors of the mean. (∗) Statistically significant increase (*$p = 1.8 \times 10^{-5}$) in sO$_2$ as compared to saline (control) treated group.

important to point out that PA imaging of sO$_2$ depends on the presence of blood flow, which is lacking in the necrotic and avascular tumor core.[30] Thus the PA images revealed sO$_2$ was mainly generated within the tumor periphery (Figure 4a). However, this does not imply that the NPs are unable to produce O$_2$ in the hypoxic region close to the tumor core, as the O$_2$ generating capacity of the NPs is limited only by the presence of H$_2$O$_2$. Interestingly, the nearly immediate detection of O$_2$ at the tumor periphery suggests the rapid distribution of the NPs within the tumor mass from the injection site (i.e., tumor center) perhaps due to the interstitial pressure gradient with a higher pressure in the tumor core than within the peripheral region.[30]

In this study, we used i.t. delivery of A-MnO$_2$ NPs for the assessment of the effect of the NPs on tumor oxygenation *in vivo*. The reason for using i.t. treatment is 2-fold. First, the local delivery method is better than systemic delivery (e.g., intravenous injection) in terms of uniformity of NP dose delivered to each tumor owing to a broad variation from tumor to tumor in morphology and NP penetration. Second, local intratumoral delivery of therapeutics has been emerging as an effective treatment of many types of localized operable and inoperable solid tumors (e.g., breast, colorectal, lung, prostate, skin, head and neck, and brain tumors) because of its advantages over systemic methods, including dramatically higher local drug concentration, better therapeutic outcomes, and minimal systemic toxic side-effects.[31,32]

Effect of A-MnO$_2$ NPs on Tumor pH. To measure intratumoral pH, we employed complementary fluorescence imaging[33] and microneedle[34] methods. We applied an established *ex vivo* tissue protocol for mapping tumor tissue pH which utilizes multispectral fluorescence imaging (MSFI) in conjunction with a pH-sensitive fluorescent dye (SNARF-4F) injected *in vivo* prior to animal sacrifice.[33] In our study, EMT6 tumor bearing animals were first injected i.t. with A-MnO$_2$ NPs, followed by intravenous injection of the SNARF-4F dye to stain for tumor pH. MSFI images of the intratumoral facets of dye-perfused tumors were then acquired

ex vivo in tissue sections and correlated to local pH from the calibration curves obtained earlier with biological tissue-like phantoms (see Supporting Information). The tumor pH was also accessed *ex vivo* with a pH microneedle probe[34] immediately after the MSFI procedure. We found that intratumoral injection of A-MnO$_2$ in orthotopic solid tumors led to higher intratumoral pH (Figure 5). After a single i.t. injection of A-MnO$_2$ NPs, the tumor pH increased, after only 20 min, from 6.2 to 6.7 (as determined by MSFI) and from 6.7 to 7.3 (as determined by microneedle probe) (Figure 5). The difference in pH values obtained with the two different methods can be attributed to interferences such as tissue autofluorescence and/or dye bleaching for MSFI images. Nonetheless, both methods revealed tumor pH values consistent with pH ranges reported in literature (e.g., pH 6.3–6.9, depending on the tumor model, cell line, and measurement method).[35] The *ex vivo* tumor tissue pH measurements (Figure 5b) revealed that A-MnO$_2$ NPs can quickly decrease tumor acidosis (i.e., within 30 min), most probably by quenching excessive protons produced by cancer cell glycolysis.[10]

Prolonged Regulation of Tumor Hypoxia, HIF-1α, and VEGF Is Related to Extended Tumor Retention of A-MnO$_2$ NPs. The extended retention of A-MnO$_2$ NPs in solid tumors is evidenced in Figure 6a. We injected near-infrared dye-labeled NPs into orthotopic EMT6 breast tumors. *In vivo* fluorescence imaging data (Figure 6a) showed substantial diffusion of NPs within the tumor tissue almost immediately after the injection and prolonged retention of NPs within the tumors for at least 24 h, followed by gradual clearance from the tumors over 24–48 h. The A-MnO$_2$ NPs are expected to be cleared as MnO$_2$ NPs which can be completely consumed by H$_2$O$_2$ (see Supporting Information Figure S3) and thereafter the remaining BSA/PAH complex is expected to undergo enzymatic degradation by specific proteases, *via* an already established mechanism for the fate of polyelectrolyte complexes taken by cells.[36,37]

We then investigated the effect of A-MnO$_2$ NPs on tumor hypoxia *in vivo* within the 24 h period post-NP-injection by immunohistochemistry to directly measure tissue hypoxia using a Pimonidazole marker[38] and the expression of HIF-1α and VEGF (Figure 6b) using antibodies. Unlike the PA experiments that measure hemoglobin-related vascular sO$_2$, the immunohistochemistry of *ex vivo* tissues from animals injected with Pimonidazole prior to sacrifice directly detects the presence of hypoxic tumor cells. We found that tumors treated with A-MnO$_2$ NPs for 30 min, 60 min, or 24 h showed 24, 45, and 37% less tissue hypoxia, respectively, as compared with the saline control (Figure 6c), suggesting a time-dependent and sustained effect of NPs on tumor hypoxia. The same tumors also showed a 19, 21, and 10% decrease in the expression of HIF-1α (Figure 6d), and 7, 65, and 65% decrease in the expression of VEGF (Figure 6e), after 30 min, 60 min, and 24 h treatment with A-MnO$_2$ NPs, respectively.
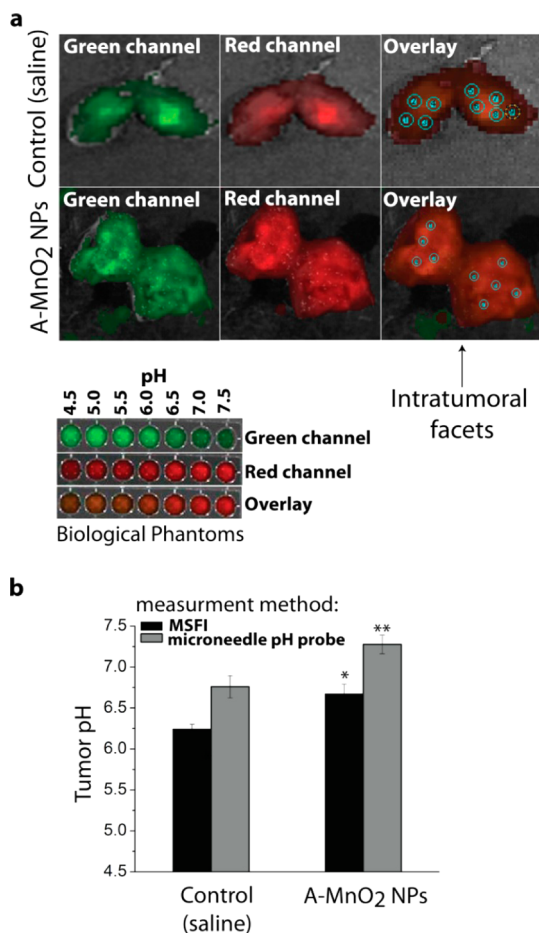

Figure 5. Effect of A-MnO$_2$ NPs on tumor pH: (a) *Ex vivo* pH imaging of solid tumors treated with i.t. injection of A-MnO$_2$ NPs or saline (control). The tumors were cut in the central line and intratumoral pH was determined with multispectral fluorescence imaging (MSFI) using a pH-sensitive fluorescent dye (SNARF-4F) and the calibration curve presented in the Supporting Information. The bottom insert shows the pH scale obtained using the dye in biological phantoms of various pH values. (b) Tumor pH after treatment with A-MnO$_2$ NPs or saline (control) (*n* = 3) determined *ex vivo* by MSFI (black bars) or with a microneedle pH probe (gray bars). Error bars represent standard errors of the mean. (∗) Statistically significant increase (*p* = 0.004, **p* = 0.007) in pH as compared to saline (control) treated group.

HIF-1α is a master regulator of the transcriptional response to acute and chronic hypoxia,[38,39] while VEGF is involved in cancer cell metabolism, angiogenesis, invasion, metastasis, and apoptosis.[40] Overexpression of VEGF is a hallmark of tumor angiogenesis.[40] On the basis of the impact of angiogenesis on cancer progression and treatment, several antiangiogenic agents including anti-VEGF molecules are now in clinical trials as a sole treatment or in combination with conventional cancer chemotherapy.[39] Thus downregulation of HIF-1α and VEGF expression would improve tumor prognosis. The results presented above show that the effectiveness of A-MnO$_2$ NPs on the regulation of the TME is not limited to the transient increase of tumor oxygenation and pH; they also have an effect on the down-regulation of hypoxia-responsive protein expression
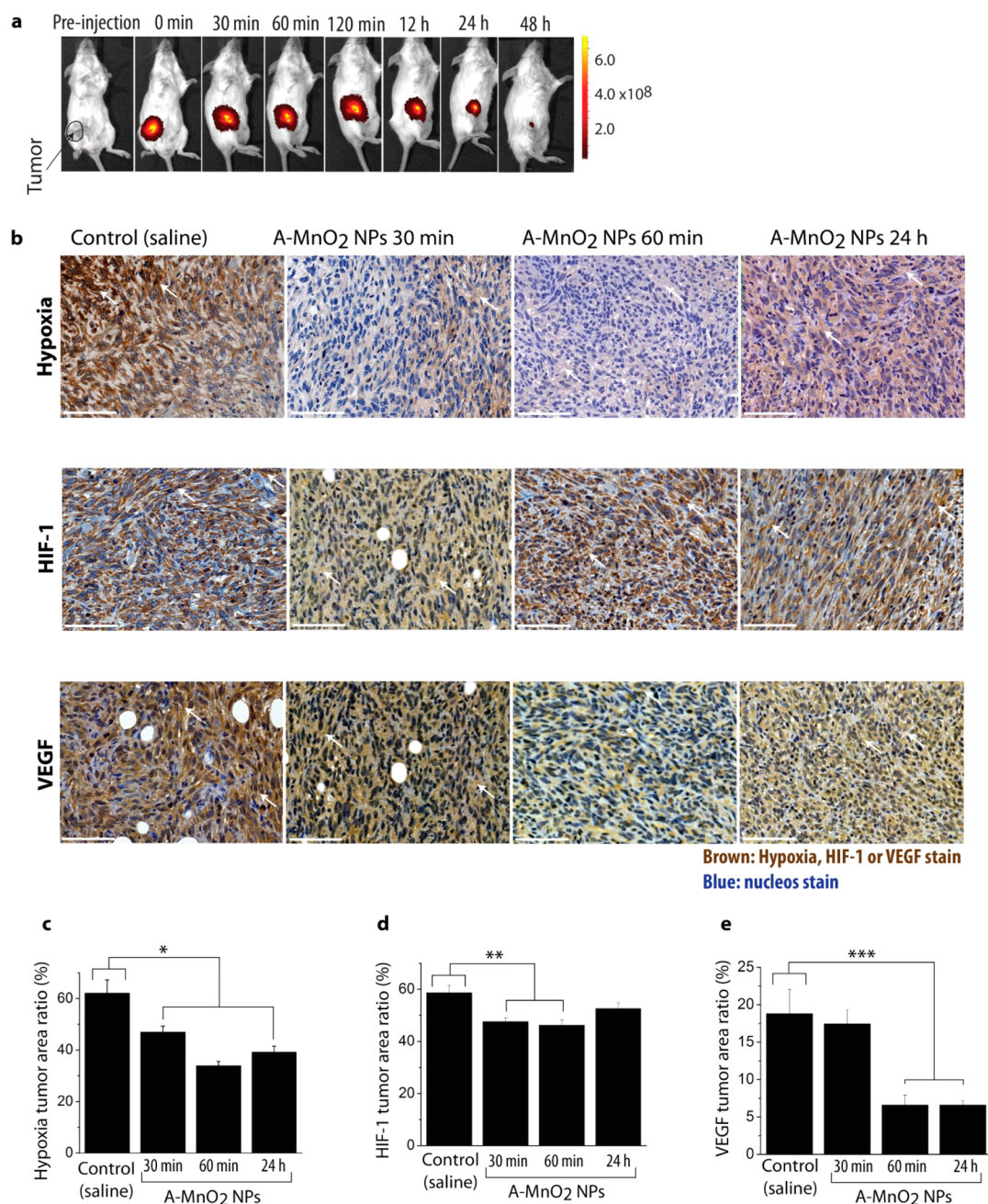
Figure 6. Tumor retention of A-MnO$_2$ NPs and effect on tumor hypoxia, HIF-1α, and VEGF. (a) Representative optical images of EMT6 tumor-bearing mouse with i.t. injected near-infrared-labeled A-MnO$_2$ NPs at various times. (b) Representative immunohistochemistry in continuous sections from EMT6 tumors treated i.t. with saline (control) or A-MnO$_2$ NPs for 30 min, 60 min and 24 h. Tumor hypoxia was determined by Pimonidazole binding HIF-1α and VEGF antibody. Scale bars correspond to 85 μm. (c−e) Quantification of tumor hypoxia, HIF-1, and VEGF after treatments, determined from classified images (not shown). (n = 3). Error bars represent standard errors of the mean. (∗) Statistically significant difference (*p = 6.9 × 10^{-5}, **p = 0.003, ***p = 4.5 × 10^{-4}) as compared to saline (control) treated group.

that plays an important role in biological behavior and therapeutic response of many types of cancers.[6,7] Because the expression of HIF-1α is transient depending on the relative rate of synthesis (*via* an O$_2$-independent pathway) and degradation (*via* an O$_2$-dependent pathway),[41] the sustained *in situ* production of O$_2$ by A-MnO$_2$ NPs is beneficial to prolonged regulation of TME especially impacting on the expression of downstream proteins, such as VEGF-4.

A-MnO$_2$ NPs Enhanced Antitumor Effect of Radiation. Various studies have shown that hypoxic cells in solid tumors are two-to-three times more resistant to a single dose of ionizing radiation than those with normal levels of oxygen.[3,4] To explore whether *in situ* oxygen production by A-MnO$_2$ NPs can enhance RT, we conducted preliminary studies in an *in vivo* orthotopic murine breast tumor model. EMT6 tumors were treated with A-MnO$_2$ NPs or saline 30 min prior to irradiation.
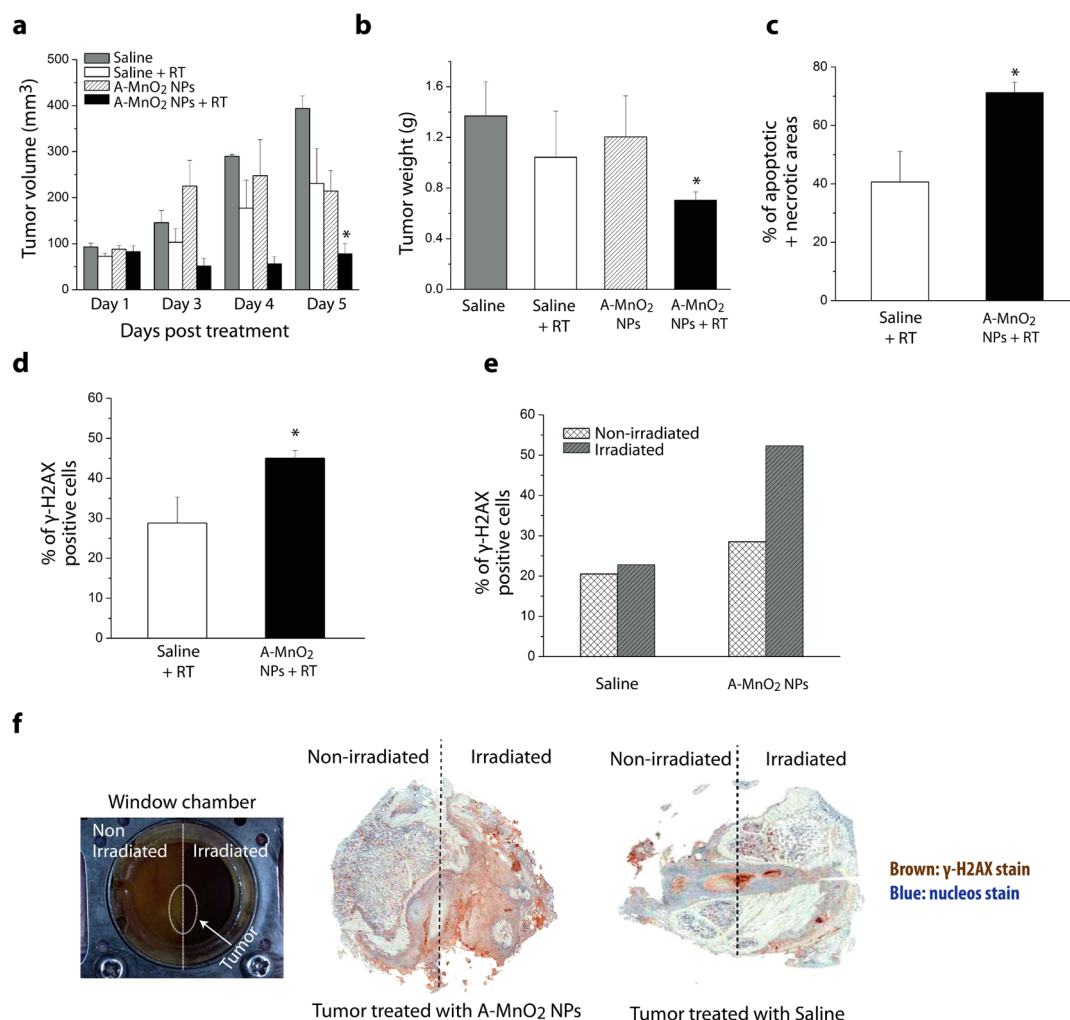
Figure 7. Effect on tumor growth after treatment with radiation and A-MnO$_2$ NPs: Tumors (n = 3/group) were treated with intratumoral injection of (1) saline, (2) saline + RT, (3) A-MnO$_2$ NP, (4) A-MnO$_2$ NP + RT. A radiation dose of 10 Gy was given 30 min after saline or A-MnO$_2$ NP treatment. (a) Tumor volume measured over time after treatment. (b) *Ex vivo* measurement of tumor weight at the end of day 5. (c) Quantification of percent necrotic + apoptotic area in tumors after treatment. (d) Quantification of DNA DSBs as measured by γ-H2AX staining in tumors after treatment. (e) Quantification of DNA DSBs determined by measuring percent of positive γ-H2AX cells in tumor tissue implanted in dorsal window chamber and treated with saline and A-MnO$_2$ NPs. (f) Representative image of tumor implanted in dorsal window chamber and treated with saline and A-MnO$_2$ NPs, and immunohistochemical image of tumor tissue stained with γ-H2AX. (∗) Statistically significant difference (*p < 0.05) as compared to all other groups.

A significant tumor growth delay was observed in mice treated with the combination of A-MnO$_2$ NPs and RT (Figure 7a) compared to the control groups. The average tumor volume in the A-MnO$_2$ NPs + RT group at day 5 remained at ~78 mm^3 while the RT alone group (treated with saline + RT) reached an average tumor volume of ~231 mm^3 at the end of day 5 after treatment. Tumor weight was also significantly lower in the A-MnO$_2$ NPs + RT group (Figure 7b). Interestingly, a decreased tumor growth was observed in the A-MnO$_2$ NP alone treated group compared to the saline group (non-irradiated controls) (Figure 7a). This moderate antitumor effect may be attributable to the manipulation of the TME by the A-MnO$_2$ NP formulation which reduces VEGF levels by 65%. A more in-depth study will be conducted in the future to further investigate this observation.

To confirm that the effect of A-MnO$_2$ NP on the enhancement of radiation response was due to tumor cell cytotoxicity, the percentage of tumor apoptotic and necrotic areas was determined. Tumors treated with A-MnO$_2$ NP + RT showed a significantly higher tumor cell death (71%) compared to the saline + RT treated group (40%) (Figure 7c). We further evaluated radiation-induced DNA double strand breaks (DNA DSBs) by using gamma H2AX staining to stain for DNA DSBs. The DNA DSB is considered the most lethal type of damage induced by ionizing radiation and is a major indicator of the efficacy of treatment.[42] Combined treatment with A-MnO$_2$ NPs and irradiation resulted in increased DNA damage (71%) compared to the saline control with irradiation (28%) in the EMT6 solid tumor (Figure 7d). A window chamber mouse model bearing tumor[43] was employed to determine the

induction of DNA DSB after treatment with radiation combined with A-MnO$_2$ NPs or saline (Figure 7e−f). Spatially localized focal X-ray irradiation was performed on half of the tissue in the transparent window chamber allowing us to determine the relative effect of treatment in the same mouse. Increased DNA DSBs were observed when the tumor was treated with both A-MnO$_2$ NP and RT versus radiation alone. Oxygen close to DNA is known to react with radiation produced radicals in DNA, "fixing" them in a state with which it is difficult for the intrinsic cellular DNA repair mechanisms to handle.[5] Therefore, it is likely that oxygen generated by the reaction of A-MnO$_2$ NP with H$_2$O$_2$ in tumor tissue facilitated the oxygen effect, causing more tumor cell death upon radiation thereby leading to an enhanced delay in tumor growth.

CONCLUSIONS

We have demonstrated a completely new and innovative application of A-MnO$_2$ NPs for the modulation of the TME. The intratumoral treatment of murine breast tumors with A-MnO$_2$ NPs resulted in simultaneous attenuation of hypoxia and acidosis in solid tumors *in vivo*. Moreover, for the first time a bioinorganic nanoparticle system has been demonstrated to promote downregulation of crucial tumor progression-related factors, that is, HIF-1α and VEGF. In addition we have demonstrated the application of A-MnO$_2$ NPs for enhancement of radiation induced tumor growth delay and cancer cell death. This work suggests a potential of the A-MnO$_2$ NP system to regulate multiple biological attributes of the TME simultaneously and to improve cancer response to radiation treatment. The *in vivo* results obtained in the present work encourage continuing efforts for the optimization and application of MnO$_2$ NPs in combination with other cancer treatments such as chemotherapy and photodynamic therapy (PDT). Such applications are the subject of future research by our group.

METHODS

Nanoparticle Synthesis. MnO$_2$ NPs were prepared by directly mixing the aqueous solutions of KMnO$_4$ and poly(allylamine hydrochloride) (PAH, 15 kDa). Briefly, 18 mL of KMnO$_4$ solution (3.5 mg mL^{-1}) was mixed with 2 mL of PAH solution (37.4 mg mL^{-1}), the mixture was left for 15 min at room temperature until all permanganate was converted to MnO$_2$. NP formation was confirmed by recording UV−vis absorption spectrum. NPs were washed three times with doubly distilled (DDI) water using ultracentrifugation (50k rpm for 1 h). This step led to small (∼15 nm) MnO$_2$ NPs stabilized with PAH. At the final step, BSA was added to the MnO$_2$ NP solution at a BSA/NP ratio 2.5% (w/w), and NaCl was added to make the solution normal saline (0.9% NaCl). This step led to the formation of A-MnO$_2$ NPs (∼50 nm), with several MnO$_2$ NPs entrapped in a PHA/BSA complex due to strong electrostatic interaction between the protein and the polymer. A typical preparation led to a ∼0.7% A-MnO$_2$ NPs solution, corresponding to ∼1.1 mM MnO$_2$ as determined by inductively coupled plasma (ICP) analysis. A-MnO$_2$ NPs were further diluted with cell medium or sterile saline for *in vitro* and *in vivo* studies, respectively. Protein labeling kits AnaTag HiLyte Fluor 594 (Texas Red) and AnaTag 750 (Anaspec Inc., USA) were used to label albumin for the preparation of red fluorescent and near-infrared NPs, respectively.

Cell Lines, Tumor Models and Treatments. *In vitro:* A murine EMT6 breast cancer cell line was utilized and cultured following standard cell culture procedures.[44] For all *in vitro* experiments, cells in αMEM medium (10^5 cells/mL) were treated with A-MnO$_2$ NPs for 1 h. Cell viability was measured using a standard MTT protocol.[44] *In vivo*: All procedures strictly complied with the ethical and legal requirements under Ontario's Animals for Research Act and the Federal Canadian Council on Animal Care guidelines for the care and use of laboratory animals and were approved by the University Animal Care Committee of the University of Toronto. Solid tumors of EMT6 breast cancer cells (10^6) were grown orthotopicly in Balb/c mice, and animals were randomly allocated for all treatments (*n* = 3/group). For *in vivo* experiments, tumors were injected with 50 μL of A-MnO$_2$ NPs solution in saline (0.2 mM MnO$_2$), which made the MnO$_2$ concentration ∼45 μM in a ∼200 mm^3 tumor. Controls were injected with an equivalent volume of sterile saline.

Quenching of H$_2$O$_2$ by Nanoparticles. For the quenching experiments, A-MnO$_2$ NPs (90 μM) was placed in cell medium containing 10% FBS at 37 °C, and H$_2$O$_2$ (1 mM) was added to initiate the reaction. The residual concentration of H$_2$O$_2$ was determined over time using a PeroXOquant assay kit (Pierce, USA), at 37 °C. Cell medium with 10% FBS was used as a vehicle control.

In vitro Oxygen and pH Measurements. O$_2$ generated by A-MnO$_2$ NPs and pH changes were measured in a semisealed chamber coupled with a MI-730 micro-oxygen electrode and MI-407 pH + MI 402 reference microelectrodes (Microelectrodes Inc., USA), at 37 °C. A-MnO$_2$ NPs were dispersed in αMEM cell medium containing 10% FBS to give various MnO$_2$ concentrations (10−90 μM). The system was made hypoxic by bubbling with N$_2$. Endogenous level of H$_2$O$_2$ (250 μM) was injected into the chamber to initiate O$_2$ generation. For experiments with hypoxic cells, Murine breast cancer EMT6 cells (10^5 cells/mL) were suspended and stirred in αMEM medium in glass vials plugged with rubber stoppers and pierced with two hypodermic needles for gassing. The cell suspension was made hypoxic by introducing a mixture of 95% N$_2$ and 5% CO$_2$ for 20 min at 37 °C. A-MnO$_2$ NPs (45 μM) were then injected, and the oxygen levels were monitored over time. For all experiments, pH or O$_2$ was monitored every 60 s using an Oakton pH 1100 (Termo Fisher Scientific Inc., USA) coupled with O$_2$-ADPT Oxygen Adapter (Microelectrodes Inc., USA) for O$_2$ measurements. All electrodes were calibrated according to manufacturer's instructions. αMEM medium with 10% FBS, with or without cells, was used as control.

Cellular Uptake of NPs. Murine EMT6 breast tumor cells (10^5 cells) were incubated for 1 h with A-MnO$_2$ NPs (45 μM) at 37 °C before microscopic analysis. Cell uptake of NPs by transmission electron microscopy (TEM) was performed using a H7000 TEM microscope (Hitachi, Japan), following standard methods for sample preparation.[45] An EVOS fluorescence microscope (AMG, USA) was used to image live cells following incubation with red fluorescent dye labeled A-MnO$_2$ NPs. Cell nuclei were stained blue with HOESCHT 33342 (Invitrogen Molecular Probes, USA).

Tumor Retention of NPs. A Xenogen IVIS Spectrum Imaging System (Caliper Life Sciences Inc., USA) was used to image tumor bearing animals over time following i.t. treatment with near-infrared labeled A-MnO$_2$ NPs. At each time point, a bright field image was acquired and fluorescence-labeled A-MnO$_2$ NPs were imaged at 754 nm excitation and 778 nm emission. Image fluorescence was quantified by equalizing the fluorescence intensity range across all images.

Tumor pH Measurements. A pH-sensitive fluorophore SNARF-4F (Life technologies S23920, USA) was used for *ex vivo* tumor pH imaging following an established protocol.[34] Tumor bearing mice were injected i.t. with NPs in saline followed by i.v. injection of the dye (1 nmol of SNARF-4F in 200 μL of sterile saline). Animals

were sacrificed 20 min following injections, tumor tissue was immediately harvested, cut in half and imaged with Xenogen IVIS Spectrum (Caliper Life Sciences Inc., USA). For control experiments, sterile saline was injected i.t. followed by intravenous (i.v.) injection of SNRAF, tumors were imaged *ex vivo* using the same conditions. All the necessary calibration curves of dye were performed following published protocols[45,46] and biological tissue-like phantoms were prepared following standard procedures[33] (see Supporting Information for details). Tumor pH was also measured using MI-407 pH + MI 402 reference microelectrodes following a standard protocol[36] (Microelectrodes Inc., USA).

Tumor Oxygenation Measurements. A Vevo LAZR Photoacoustic Imaging System (VisualSonics Inc., Canada) with a 21 MHz center frequency transducer (LZ-550, VisualSonics Inc., Canada) was used to measure vascular oxygen saturation (sO_2) *in situ* over time before and after i.t. treatment with A-MnO$_2$ NPs. Ultrasound was utilized to guide NP injection in order to administer treatments to the tumor. Animals were maintained below 7% oxygen atmosphere during the experiment and sO_2 measurements were assessed using standard multispectral photoacoustic imaging in the tumors *in vivo* using two excitation wavelengths (750 and 850 nm) for deoxygenated and oxygenated hemoglobin, respectively.

Immunohistochemistry Detection of Tumor Hypoxia. The hypoxia marker Pimonidazole hydrochloride (Hypoxyprobe-1 plus kit, Hypoxyprobe Inc., USA) was used for *ex vivo* tissue staining of hypoxia following the protocol provided with the kit. Rabbit polyclonal HIF-1α antibody (dilution 1:100, Novus Biologicals, catalog number NB100-134) and Rabbit anti-VEGF (dilution 1:100, Thermo Scientific, catalog number ab-222-P) were used for the staining of HIF-1α and VEGF, respectively. Briefly, tumor bearing mice ($n = 3$/group) were treated i.t. with A-MnO$_2$ NPs or saline (control). After predetermined times animals were sacrificed and tumor tissues were harvested and fixed with 10% neutral buffered formalin solution (Sigma Aldrich, USA) for histological analysis. Tumor tissue preparation and analysis were performed by the CMHD Pathology Core laboratory at Mount Sinai Hospital, Toronto. Slides were scanned with a NanoZoomer 2.0 RS whole slide scanner (Hamamatsu, Japan) and images were analyzed with Visiopharm 4.4.4.0 software.

In Vivo Radiation Treatment. Solid tumor of EMT6 murine breast cancer cells were grown orthotopically in Balb/c mice. Mice were divided into four groups ($n = 3$/group): (1) saline, (2) saline + RT, (3) A-MnO$_2$ NP, (4) A-MnO$_2$ NP + RT. Treatments were initiated when the tumors reached an approximate volume of 100 mm^3. The mice were restrained in a specially designed acrylic box, and the tumors were irradiated locally with 10 Gy, 30 min after i.t administration of saline or A-MnO$_2$ NP. The tumor size was measured as a function of time with vernier calipers in two dimensions and tumor volumes were calculated by the formula $V = [(\text{length}) \times (\text{width})^2]/2$. At the end of experiment, the animals were sacrificed and the tumor masses were excised and weighed. Tumor tissue was also formalin fixed and stained with terminal deoxynucleotidyl transferase dUTP nick end labeling (TUNEL) and hematoxylin and eosin (H&E) to determine percent apoptosis and necrosis.

In another set of experiments, mice were sacrificed 24 h after radiation treatment. Tumor tissue was excised, formalin fixed, sectioned, and gamma H2AX was measured to evaluate DNA DSBs. Slides were scanned with a NanoZoomer 2.0 RS whole slide scanner (Hamamatsu, Japan), and images were analyzed with Visiopharm 4.4.4.0 software.

The enhancement of DNA DSBs due to the combination of RT + A-MnO$_2$ NP was also evaluated in a dorsal skin-fold window chamber (DSWC) EMT6 mouse model.[43] Treatments (saline and A-MnO$_2$ NP) were injected i.t. and only half of the chamber was irradiated at 10 Gy. Irradiating only half of the chamber allowed us to determine the effect of treatment alone in the same mice. Twenty-four hours postirradiation tumor tissue was excised and stained with gamma H2AX staining to evaluate DNA DSBs. Slides were scanned and images were analyzed with Visiopharm 4.4.4.0 software.

Statistical Analysis. Data are presented as mean ± standard error of the mean for results obtained from three independent trials unless otherwise indicated. Student's *t* test or analysis of variance (ANOVA) followed by Tukey *t* test (OriginPro8) was utilized to determine statistical significance between two or more groups, respectively. *p*-Values < 0.05 were considered statistically significant.

Conflict of Interest: The authors declare no competing financial interest.

REFERENCES AND NOTES

1. Gatenby, R. A.; Gillies, R. J. A Microenvironmental Model of Carcinogenesis. *Nat. Rev. Cancer* **2008**, *8*, 56–61.
2. Rockwell, S.; Dobrucki, I. T.; Kim, E. Y.; Marrison, S. T.; Vu, V. T. Hypoxia and Radiation Therapy: Past History, Ongoing Research, and Future Promise. *Curr. Mol. Med.* **2009**, *9*, 442–458.
3. Lundgren, K.; Holm, C.; Landberg, G. Hypoxia and Breast Cancer: Prognostic and Therapeutic Implications. *Cell. Mol. Life Sci.* **2007**, *64*, 3233–3247.
4. Vaupel, P.; Schlenger, K.; Knoop, C.; Hockel, M. Oxygenation of Human Tumors: Evaluation of Tissue Oxygen Distribution in Breast Cancers by Computerized O$_2$ Tension Measurements. *Cancer Res.* **1991**, *51*, 3316–3322.
5. Bertout, J. A.; Patel, S. A.; Simon, M. C. The Impact of O$_2$ Availability on Human Cancer. *Nat. Rev. Cancer* **2008**, *8*, 967–975.
6. Rademakers, S. E.; Span, P. N.; Kaanders, J. H.; Sweep, F. C.; van der Kogel, A. J.; Bussink, J. Molecular Aspects of Tumour Hypoxia. *Mol. Oncol.* **2008**, *2*, 41–53.
7. Semenza, G. Hypoxia-Inducible Factors: Mediators of Cancer Progression and Targets of Cancer Therapy. *Trends Pharmacol. Sci.* **2012**, *33*, 207–214.
8. Liao, D.; Johnson, R. S. Hypoxia: A Key Regulator of Angiogenesis in Cancer. *Cancer Metastasis Rev.* **2007**, *26*, 281–290.
9. Forsythe, J. A.; Jiang, B. H.; Iyer, N. V.; Agani, F.; Leung, S. W.; Koos, R. D.; Semenza, G. L. Activation of Vascular Endothelial Growth Factor Gene Transcription by Hypoxia-Inducible Factor 1. *Mol. Cell. Biol.* **1996**, *16*, 4604–4613.
10. Gatenby, R. A.; Gillies, R. J. Why Do Cancers Have High Aerobic Glycolysis? *Nat. Rev. Cancer.* **2004**, *4*, 891–899.
11. Chiche, J.; Brahimi-Horn, M. C.; Pouysségur, J. Tumour Hypoxia Induces a Metabolic Shift Causing Acidosis: A Common Feature In Cancer. *J. Cell Mol. Med.* **2010**, *14*, 771–794.
12. López-Lázaro, M. Dual Role of Hydrogen Peroxide in Cancer: Possible Relevance to Cancer Chemoprovention and Therapy. *Cancer Lett.* **2007**, *252*, 1–8.
13. Hellman, S. Principles of Cancer Management: Radiation Therapy. In *Principles & Practice of Oncology*, 5th ed.; Devita, V. T., Jr., Hellman, S., Rosenberg, S. A., Eds.; Lippincott-Raven Publishers: Philadelphia, 1997; pp 307−331.
14. Wu, W.; Yang, Q.; Li, T.; Zhang, P.; Zhou, R.; Yang, C. Hemoglobin-Based Oxygen Carriers Combined with Anticancer Drugs May Enhance Sensitivity of Radiotherapy and Chemotherapy to Solid Tumors. *Artif. Cells Blood Substit. Immobil. Biotechnol.* **2009**, *37*, 163–165.
15. Overgaard, J.; Horsman, M. R. Modification of Hypoxia Induced Radioresistance in Tumors by the Use of Oxygen and Sensitizers. *Semin. Radiat. Oncol.* **1996**, 10–12.
16. Gordijo, C. R.; Shuhendler, A. J.; Wu, X. Y. Glucose-Responsive Bio-Inorganic Nanohybrid Membrane or Self-Regulated Insulin Release. *Adv. Funct. Mater.* **2010**, *20*, 1404–1412.

17. Luo, X. L.; Xu, J. J.; Zhao, W.; Chen, H. Y. A Novel Glucose ENFET Based on the Special Reactivity of MnO$_2$ Nanoparticles. *Biosens. Bioelectron.* **2004**, *19*, 1295–1300.

18. Yildirimer, L.; Thanh, N. T. K.; Loizidou, M.; Seifalian, A. M. Toxicological Considerations of Clinically Applicable Nanoparticles. *Nano Today.* **2011**, *6*, 585–607.

19. Bai, Y.; Du, Y.; Xu, J. Choline Biosensors Based on a Bi-electrocatalytic Property of MnO$_2$ Nanoparticles Modified Electrodes to H$_2$O$_2$. *Electrochem. Commun.* **2007**, *9*, 2611–2616.

20. Liu, X.; Wang, Q.; Zhao, H.; Zhang, L.; Su, Y.; Lv, Y. BSA-Templated MnO$_2$ Nanoparticles as Both Peroxidase and Oxidase Mimics. *Analyst* **2012**, *137*, 4552–4558.

21. Luo, Y. Preparation of MnO$_2$ Nanoparticles by Directly Mixing Potassium Permanganate and Polyelectrolyte Aqueous Solutions. *Mater. Lett.* **2007**, *61*, 1893–1895.

22. Kaibara, K.; Okazaki, T.; Bohidar, H. B.; Dubin, P. L. pH-Induced Coacervation in Complexes of Bovine Serum Albumin and Cationic Polyelectrolytes. *Biomacromolecules* **2000**, *1*, 100–107.

23. Alkilany, A. M.; Nagaria, P. K.; Hexel, C. R.; Shaw, T. J.; Murphy, C. J.; Wyatt, M. D. Cellular Uptake and Cytotoxicity of Gold Nanorods: Molecular Origin of Cytotoxicity and Surface Effects. *Small* **2009**, *5*, 701–708.

24. Halliwell, B.; Clement, M. V.; Long, L. H. Hydrogen Peroxide in the Human Body. *FEBS Lett.* **2000**, *486*, 10–13.

25. Desai, N. Nab Technology: A Drug Delivery Platform Utilizing Endothelial Gp60 Receptor-Based Transport and Tumour-Derived SPARC for Targeting. *Drug Delivery Rep.* **2007**, No.), 37–41.

26. Desai, N. Nanoparticle Albumin Bound (*NAB*) Technology: Targeting Tumors through the Endothelial Gp60 Receptor and SPARC. *Nanomed.: Nanotechnol., Biol. Med.* **2007**, *3*, 339.

27. Desai, N.; Trieu, V.; Damascelli, B.; Soon-Shiong, P. SPARC Expression Correlates with Tumor Response to Albumin-Bound Paclitaxel in Head and Neck Cancer Patients. *Transl. Oncol.* **2009**, *2*, 59–64.

28. Desai, N.; Trieu, V.; Yao, Z.; Louie, L.; Ci, S.; Yang, A.; Tao, C.; De, T.; Beals, B.; Dykes, D.; et al. Increased Antitumor Activity, Intratumor Paclitaxel Concentrations, and Endothelial Cell Transport of Cremophor-Free, Albumin-Bound Paclitaxel, ABI-007, Compared with Cremophor-Based Paclitaxel. *Clin. Cancer Res.* **2006**, *12*, 1317–1324.

29. Zhang, H. F.; Maslov, K.; Stoica, G.; Wang, L. V. Functional Photoacoustic Microscopy for High Resolution and Noninvasive *in Vivo* Imaging. *Nat. Biotechnol.* **2006**, *34*, 848–851.

30. Fukumura, D.; Duda, D. G.; Munn, L. L.; Jain, R. K. Tumor Microvasculature and Microenvironment: Novel Insights through Intravital Imaging in Pre-clinical Models. *Microcirculation* **2010**, *17*, 206–225.

31. Goldberg, E. P.; Hadba, A. R.; Almond, B. A.; Marotta, J. S. Intratumoral Cancer Chemotherapy and Immunotherapy: Opportunities for Nonsystemic Preoperative Drug Delivery. *J. Pharm. Pharmacol.* **2002**, *54*, 159–180.

32. Yang, L.; Wang, B.; Qiao, W.; Liu, P. A Novel Combination Chemotherapy Integrating with Intratumoral Chemotherapy. *Med. Hypotheses* **2009**, *73*, 334–335.

33. Hight, M. R.; Nolting, D. D.; McKinley, E. T.; Lander, A. D.; Wyatt, S. K.; Gonyea, M.; Zhao, P.; Manning, H. C. Multispectral Fluorescence Imaging to Assess pH in Biological Specimens. *J. Biomed. Opt.* **2011**, *16*, 0160071–7.

34. Kalliomaki, T.; Hill, R. P. Effects of Tumour Acidification with Glucose + MIBG on the Spontaneous Metastatic Potential of Two Murine Cell Lines. *Br. J. Cancer* **2004**, *90*, 1842–1849.

35. Gillies, R. J.; Raghunand, N.; Garcia-Martin, M. L.; Gatenby, R. A. pH Imaging—A Review of pH Measurement Methods and Applications in Cancers. *IEEE Eng. Med. Biol. Mag.* **2004**, *23*, 57–64.

36. Peyratout, C. S.; Dahne, L. Tailor-Made Polyelectrolyte Microcapsules: From Multilayers to Smart Containers. *Angew. Chem., Int. Ed.* **2004**, *43*, 3762–3783.

37. Rivera-Gill, P.; De Koker, S.; De Geest, B. G.; Parak, W. J. Intracellular Processing of Proteins Mediated by Biodegradable Polyelectrolyte Capsules. *ACS Nano* **2009**, *9*, 4398–4402.

38. Rademakers, S. E.; Lok, J.; van der Kogel, A. J.; Bussink, J.; Kaanders, J. H. Metabolic Markers in Relation to Hypoxia; Staining Patterns and Colocalization of Pimonidazole, HIF-1α, CAIX, LDH-5, GLUT-1, MCT1 and MCT4. *BMC Cancer.* **2011**, *11*, 167–177.

39. Wu, H.; Huang, C.; Chang, D. Anti-angiogenic Therapeutic Drugs for Treatment of Human Cancer. *J. Cancer Mol.* **2008**, *4*, 37–45.

40. Carmeliet, P.; Jain, R. K. Angiogenesis in Cancer and Other Diseases. *Nature* **2000**, *407*, 249–257.

41. Moroz, E.; Carlin, S.; Dyomina, K.; Burke, S.; Thaler, H. T.; Blasberg, R.; Serganova, I. Real Time Imaging of HIF-1α Stabilization and Degradation. *PLoS ONE* **2009**, *4*), 1–13.

42. Emil, M.; Simon, M.; Aashish, S.; George, I. DNA Double-Strand Break Repair as Determinant of Cellular Radiosensitivity to Killing and Target in Radiation Therapy. *Front. Oncol.* **2013**, 1–18.

43. Maeda, A.; Leung, M. K. K.; Conroy, L.; Chen, Y.; Bu, J.; Lindsay, P. E.; Mintzberg, S.; Virtanen, C.; Tsao, J.; Winegarden, N. A.; et al. *In Vivo* Optical Imaging of Tumor and Microvascular Response to Ionizing Radiation. *PLoS ONE* **2012**, *7*), 1–15.

44. Shalviri, A.; Raval, G.; Prasad, P.; Chan, C.; Liu, Q.; Heerklotz, H.; Rauth, A. M.; Wu, X. Y. pH-Dependent Doxorubicin Release from Terpolymer of Starch, Polymethacrylic Acid and Polysorbate 80 Nanoparticles for Overcoming Multi-Drug Resistance in Human Breast Cancer Cells. *Eur. J. Pharm. Biopharm.* **2012**, *82*, 587–597.

45. Zhang, F.; Ali, Z.; Amin, F.; Feltz, A.; Oheim, M.; Parak, W. J. Ion and pH Sensing with Colloidal Nanoparticles: Influence of Surface Charge on Sensing and Colloidal Properties. *Chemphyschem.* **2010**, *11*, 730–735.

46. del Mercato, L. L.; Abbasi, A. Z.; Parak, W. J. Synthesis and Characterization af Ratiometric Ion-Sensitive Polyelectrolyte Capsules. *Small* **2011**, *7*, 351–363.